

Phase-field study of eutectic colony formation in NiAl-34Cr

Michael Kellner^{a,b,*}, Johannes Hötzer^{a,b}, Ephraim Schoof^a, Britta Nestler^{a,b}

^a*Institute for Applied Materials (IAM), Karlsruhe Institute of Technology (KIT), Straße
am Forum 7, 76131 Karlsruhe, Germany*

^b*Institute of Digital Materials Science, Karlsruhe University of Applied Sciences,
Moltkestrasse 30, 76133 Karlsruhe, Germany*

Abstract

The formation of two-phase eutectic colonies is often observed in microstructures of directionally solidified ternary alloys. Their formation is driven by microscopic instabilities in a macroscopic planar solidification front, due to impurities of the minor component, diffusing from the two solidifying phases into the liquid. The growth conditions for eutectic colonies, their interactions and their responses to the microstructure during growth are the focus of the current work. Therefore, phase-field simulations based on a grand potential formalism are performed for the high-performance material NiAl-34Cr. To enable the evolution of eutectic colonies in two-dimensional simulations, a concentration-driven nucleation mechanism is introduced into a multiphase-field framework and is subsequently validated. With this mechanism, two-dimensional large-scale phase-field simulations are conducted to study the influence of the applied temperature gradient on the evolving colonies. The patterns are quantitatively analyzed by measuring their number, size and height. Furthermore, the adjustment processes between the eutectic colonies during the directional solidification are investigated. The results demonstrate the ability of the presented phase-field approach with integrated nucleation mechanism for the formation of eutectic colonies in two-dimensional simulations.

*Corresponding author. Tel.: +49 721 608-41452; Fax: +49 721 608-45024; email: michael.kellner@kit.edu

Keywords: Phase-field simulation, Nucleation, Eutectic Colonies, Directional solidification, Jackson-Hunt analysis, NiAl-34Cr

1. Introduction

During the directional solidification of eutectic multicomponent alloys, eutectic colonies can evolve in the microstructure under certain conditions of the composition and temperature. Due to the different compositions of the solidifying phases, a concentration accumulation of some alloy components can be observed in the melt ahead of the solidifying phases. Depending on the growth velocity, the temperature gradient and the composition, the impurities form differently strong accumulations ahead of the solid phases. An increasing amount of impurities can lead to an instability of the planar solidification front, breaking up into cells/colonies [1, 2]. This impurity-driven Mullins-Sekerka instability [3–6], in which parts of the front are preferred to grow, can lead to the formation of eutectic colonies. Thereby, the eutectic fibers and lamellae do not only evolve along the direction of the temperature gradient, but also tilted to the growth direction. Due to the tilting, a curved solidification front forms and the lamellar spacing spreads. This can lead to the formation of new lamellae, to establish a reduced spacing, following the Jackson-Hunt criterion [7]. Hence, a eutectic colony consists of multiple eutectic fibers or lamellae, which can be several times smaller than the colony itself.

Raj and Locci [8] investigated experimentally the size of colonies depending on the growth rate for the system Ni-Al-Cr-Mo. For increasing velocities, more colonies with similar sizes are found, whereas the size distribution of the colonies is larger and fewer colonies are found for lower velocities. Further experimental works for the systems MnSb-(Sb,Bi) and MnSb-(Sb,Sn) are presented in [9] as well as for the system Al-Ag-Cu in [10].

A theory for the growth behavior of eutectic colonies, also known as two-phase eutectic cells, is proposed by Himemiya [11]. With this model, cellular-eutectic and dendritic-eutectic growth can be distinguished and a phase selection

map can be derived along the eutectic groove. In their pioneer theoretical work [12] from 1999, Plapp and Karma describe the initial stages of eutectic colony formation. Therefore, they use a linear stability analysis of the thin lamellar eutectic interface in the presence of a ternary impurity.

In 2002, they continued their work [12] by comparing their theory with 2D large-scale simulations of Al-Ag-Cu, using an isotropic phase-field model [13]. Lahiri and Choudhury [14] extended this model [13] to consider the anisotropy of the solid-solid and solid-liquid interfaces. Thus, the effect of the growth fronts in multiphase alloys is studied. In their work, the system evolves to a fixed colony spacing, which is not observed for isotropic systems. Further studies with the phase-field method and stability analysis were conducted by Lan and co-workers [15–18], who classified different shapes of the formations, depending on the growth velocity and the cell spacing. A special arrangement of eutectic colonies are spiral dendrites, which are investigated simulatively with the phase-field method by Pusztai et al. [19]. Besides the visual accordance between the experimental results and the simulations, a scaling of the tip radius with the interface free energy and the kinetic anisotropy is found. The influence of the surface energy anisotropies on the formation of two-phase spiral dendrites is further examined by Ratkai et al. in [20]. They conclude that an observation of this type of formation without anisotropy is unlikely, in contrast to the expectations of Akamatsu et al. [21, 22]. A summary of the work in the field of eutectic colonies is provided in [23].

The focus of this work is to numerically investigate the evolution of eutectic colonies with the phase-field method, depending on the applied temperature gradient. To resolve the different scales between the eutectic and the colony structure simultaneously in one simulation, large simulation domains with a high resolution are required. To reduce the required computational effort, only two-dimensional large-scale simulations are conducted. Therefore, the grand potential model of Hötzer et al. [24], which has proven to be suitable for efficiently performing large-scale simulations, serves as a starting point. For the evolution of a eutectic colony, the occurrence of new lamellae is needed. The formation of

new lamellae is generally driven by splitting or nucleation events of the phases.

60 As shown in [25], the adjustment of eutectic microstructures is mainly driven by splitting and merging events. In two-dimensional simulations, however, a splitting event can only occur in conjunction with a nucleation event. To enable the investigation of eutectic colonies in 2D, the aforementioned model is extended by a kinetically consistent concentration-driven nucleation mechanism.

65 Modeling nucleation, however, is one of the main challenges in phase-field approaches [26]. Especially in a multiphase-field framework, where only the active phase-fields are updated, special treatments have to be incorporated to trigger nucleation. In general, this can be done by an explicit nucleation method where nuclei are set according to a seed density model [27] or by applying a
70 noise to the phase-fields, as it is done in [28], for example. The second one is especially appropriate for highly unstable systems, i.e., for conditions where a small perturbation from the metastable state results in a nucleation of the thermodynamically more stable phase. Therefore, the second approach is used in this work. Nestler and Wheeler [29] investigated the adjustment of a eutectic
75 lamellar spacing in an unstable regime, as an effect of the spontaneous nucleation of solids in liquid. An overview of the works studying nucleation mechanisms with the phase-field method is given in [30].

To ensure the thermodynamic consistence of the simulations, the ternary system Ni-Al-Cr is used for the investigations. The directionally solidified eutectic alloy NiAl-34Cr possesses promising properties for structural applications at
80 high temperatures, such as an increased creep resistance, compared to the intermetallic NiAl, while keeping the excellent oxidation behavior of the binary compound. With its high melting point ($T_m = 1911$ K), its low density (5.95 g/cm³), its high thermal conductivity (> 70 W/Km) and its excellent oxidation resistance,
85 NiAl is of particular interest for technical applications at elevated temperatures, such as turbine blades in jet engines or stationary gas turbines [31, 32]. Apart from these advantages, NiAl possesses a low fracture toughness and ductility at room temperature as well as insufficient strength at high temperatures and a poor creep resistance [33]. One possible way to overcome these disadvantages

90 is to introduce a second reinforcing phase, through the addition of refractory
 metals (e.g. Cr, Mo and W) [34] and through the subsequent directional solid-
 ification of the resulting quasi-binary eutectics. The ternary system Ni-Al-Cr
 contains a binary eutectic reaction at 34 at.% Cr, 33 at.% Ni and 33 at.% Al,
 between the liquid and the two solid phases NiAl (ordered B2) and Cr (disor-
 95 dered A2) [35, 36]. A quantitative comparison between experimental samples
 and large-scale phase-field simulations of the system NiAl-34Cr for different so-
 lidification velocities is reported in [37]. During the directional solidification,
 Cr-rich fibers grow in a hexagonal arrangement, embedded in a NiAl-matrix.
 The influence of changing solidification velocities on the adjustment processes
 100 of the fibers into a hexagonal arrangement is investigated in [38]. Depending on
 the process conditions and the melt composition, differently strong amounts of
 impurity-driven Mullins-Sekerka instabilities can be observed, which can result
 in the formation of eutectic colonies.

In the following, the basic phase-field model, the extended nucleation mech-
 105 anism and the used simulation setup is presented. Subsequently, the nucleation
 mechanism is adjusted and validated. Based on this, two-dimensional large-
 scale simulations are conducted to investigate the influence of the temperature
 gradient on the colony shapes and sizes. In addition, the interactions between
 colonies during their evolution are studied. Finally, the results are summarized
 110 and discussed.

2. Method

For the investigation of the two-phase eutectic reaction $Liquid \rightleftharpoons B2_{NiAl} + A2_{Cr}$
 in the ternary system Ni-Al-Cr, a thermodynamically consistent phase-field
 model based on a grand potential functional is used [24, 39, 40]. The $N = 3$
 phases are represented by the order parameters $\phi_{\hat{\alpha}}$ and describe the local phase
 fractions. The $K = 3$ chemical potential vectors $\boldsymbol{\mu}$ are derived from the mass
 balance of the concentrations and from Fick's law. The coupling of the N phase-
 fields, the K chemical potentials and the imprinted temperature T , results in

the following set of evolution equations:

$$\begin{aligned} \tau \varepsilon \frac{\partial \phi_{\hat{\alpha}}}{\partial t} &= -\varepsilon \underbrace{\left(\frac{\partial a(\phi, \nabla \phi)}{\partial \phi_{\hat{\alpha}}} - \nabla \cdot \frac{\partial a(\phi, \nabla \phi)}{\partial \nabla \phi_{\hat{\alpha}}} \right)}_{:= r h s_{1, \hat{\alpha}}} - \frac{1}{\varepsilon} \frac{\partial \omega(\phi)}{\partial \phi_{\hat{\alpha}}} \\ &\quad - \underbrace{\frac{\partial \psi(\phi, \boldsymbol{\mu}, T)}{\partial \phi_{\hat{\alpha}}}}_{:= r h s_{2, \hat{\alpha}}} - \underbrace{\frac{1}{\tilde{N}} \sum_{\hat{\beta}=1}^{\tilde{N}} (r h s_{1, \hat{\beta}} - r h s_{2, \hat{\beta}})}_{\Lambda}, \end{aligned} \quad (1)$$

$$\begin{aligned} \frac{\partial \boldsymbol{\mu}}{\partial t} &= \left[\sum_{\hat{\alpha}=1}^N h_{\hat{\alpha}}(\phi) \left(\frac{\partial \mathbf{c}_{\hat{\alpha}}(\boldsymbol{\mu}, T)}{\partial \boldsymbol{\mu}} \right) \right]^{-1} \left(\nabla \cdot (\mathbf{M}(\phi, \boldsymbol{\mu}, T) \nabla \boldsymbol{\mu} - \mathbf{J}_{\text{at}}(\phi, \boldsymbol{\mu}, T)) \right) \\ &\quad - \sum_{\hat{\alpha}=1}^N \mathbf{c}_{\hat{\alpha}}(\boldsymbol{\mu}, T) \frac{\partial h_{\hat{\alpha}}(\phi)}{\partial t} - \sum_{\hat{\alpha}=1}^N h_{\hat{\alpha}}(\phi) \left(\frac{\partial \mathbf{c}_{\hat{\alpha}}(\boldsymbol{\mu}, T)}{\partial T} \right) \frac{\partial T}{\partial t}, \end{aligned} \quad (2)$$

$$\frac{\partial T}{\partial t} = \frac{\partial}{\partial t} (T_0 + G(x - v_G t)) = -G v_G. \quad (3)$$

The parameter τ in (1) is introduced to relate the different timescales of the evolution equations. The shape of the diffuse interface between the phases is modeled by the gradient energy term $a(\phi, \nabla \phi)$, the obstacle potential term $\omega(\phi)$ and the parameter ε , which controls the interface width. The driving force for the phase transition is described by the difference of the grand potentials, which are modeled in the term $\psi(\phi, \boldsymbol{\mu}, T)$. The grand potentials are calculated from the Gibbs energies g of the obtained $N = 3$ phases. The Gibbs energies are incorporated from the thermodynamic CALPHAD database of Peng et al. [41], to ensure the thermodynamic consistency of the model. To reduce the computational effort, the thermodynamic data is fitted by a parabolic approach of the form:

$$g_{\hat{\alpha}}(\mathbf{c}, T) = \langle \mathbf{c}, \boldsymbol{\Xi}_{\hat{\alpha}}(T) \mathbf{c} \rangle + \langle \mathbf{c}, \boldsymbol{\xi}_{\hat{\alpha}}(T) \rangle + X_{\hat{\alpha}}(T), \quad (4)$$

with the matrix $\boldsymbol{\Xi}_{\hat{\alpha}}(T)$, the vector $\boldsymbol{\xi}_{\hat{\alpha}}(T)$, the scalar $X_{\hat{\alpha}}(T)$ and the scalar product $\langle \cdot, \cdot \rangle$ [37, 42]. The approximated Gibbs energy function (4) depends on the concentration vector c and the temperature T . The last part of (1) is the
115 Lagrange multiplier Λ , with \tilde{N} as the number of locally active phases. The multiplier is introduced to fulfill the constraint $\sum_{\hat{\alpha}=1}^N \partial \phi_{\hat{\alpha}} / \partial t = 0$ [43]. The evolution equation of the chemical potentials is given in (2), with the mobility term \mathbf{M} ,

the anti-trapping current \mathbf{J}_{at} [40, 44, 45] and the interpolation function h_α [46]. Following the initially imprinted temperature function (3), with the base temperature T_0 , the temperature T evolves in the growth direction x depending on the gradient G and the velocity v_G . The partial differential equations (1) to (3) are spatially discretized with finite differences and the temporal evolution is calculated with a forward Euler scheme [47]. These numerical solution schemes are implemented into the massively parallel multiphysics framework PACE3D [48]. A more detailed description of the general phase-field model is presented in [24].

For a simultaneous resolution of the fibrous structure of the eutectic NiAl-34Cr and the multiple times larger structures of the eutectic colonies in one simulation, large solidification fronts with a high resolution are needed. As the formation of colonies is an instability-driven process, long simulation runs with multiple million iteration steps are necessary as well. Therefore, large-scale 2D simulations are performed to investigate colony formation and colony interplay. To resolve similar structures in representative three-dimensional volume elements, more than 10^8 CPUh would be required in relation to the used parameters, described in AppendixA.

For the evolution of new rods, which is required to ensure a stable growth of curved solidification fronts with multiple phases in 2D phase-field simulations, the possibility of solid phase nucleation has to be given. Following the approach from Schoof et al. [28], which showed successful nucleation for martensitic phase transformation in the context of a comparable multiphase-field evolution equation, the presented model is extended by a nucleation mechanism. To introduce new nuclei into the simulations, a noise term ζ_α is added to the phase-field evolution equation. The term has the form

$$\zeta_\alpha = \begin{cases} n_{\text{dist}} \cdot A & \forall \phi_\beta \phi_l > 0, \quad t_{\text{step}} \bmod i = 0 \\ 0, & \text{else} \end{cases} \quad (5)$$

and is used in the solid-liquid interface to enable the evolution of new rods. The generally uniform distribution of the noise is given by the function n_{dist} . The parameter A describes the amplitude, ϕ_l is the value of the order param-

eter for the liquid phase, t_{step} describes the time step of the simulation and i is the interval at which the noise term interferes. The nucleation mechanism fulfills the conditions $\sum_{\alpha} \phi_{\alpha} = 1$ and $c_{\text{new}} = c_{\text{old}}$ for each cell of the simulation domain. However, due to the nucleation of a new phase, the chemical potentials in the considered cells have to change to ensure a thermodynamic consistence. Hence μ_{new} is not equal to μ_{old} . With each nucleation iteration, multiple nuclei are randomly set into the solid-liquid interface. As a modification to [28], only favorable regions of the interface in which a set nucleus can grow and form a new stable phase, are chosen for the nucleation. Based on experimental observations [1, 2], the magnitude of the concentration accumulations ahead of the solidification front is used as criterion for a favorable region.

In each nucleation step, the concentrations in the interface between the solids and the liquid are determined to identify the deviation of the evolved concentrations from the equilibrium state. If the concentration of a cell in the interface exceeds a predefined limit, the nucleation mechanism is implementing the noise function into the cell. As the concentration of one cell does not differ strongly from the concentration of the surrounding cells, spatial compact areas are influenced by the noise function, leading to stable nuclei with a clear bulk region.

In Fig. 1, the concentration limits c_{limits} for the nucleation mechanism in NiAl-34Cr are schematically depicted. The colored triangles and the square symbol respectively indicate the equilibrium concentrations of the two solid phases and the liquid. The concentration deviations in front of the two solid phases are marked with correspondingly colored circles, along the lever arms, from the liquid equilibrium concentration to the solids. The concentration limits are marked by red lines and are determined from the deviations of the accumulated concentrations c_{der} in fraction of the referring lever arm. For a better visualization, an unnaturally enlarged deviation of 20% ($c_{\text{der}} = 0.2$) is used in Fig. 1.

165

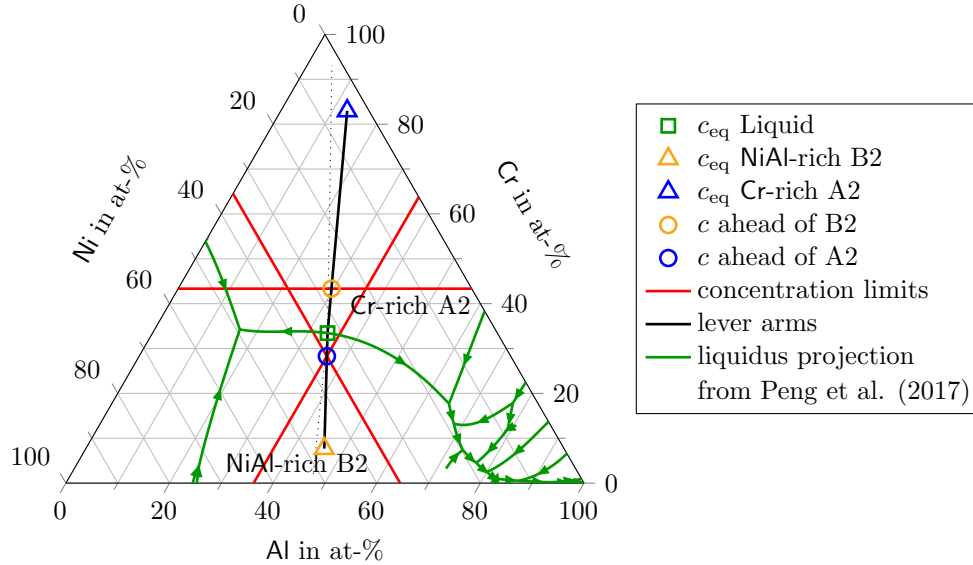


Figure 1: Liquidus projection of Ni-Al-Cr from Peng et al. [41] (green lines), with equilibrium concentrations of the solids (triangles) and liquid (square), lever arms (black lines), concentrations ahead of the solidifying phases (circles) and concentration limits (red lines) for a deviation of $1/5$, to adjust the nucleation mechanism.

3. Setup

To investigate the evolution of eutectic colonies, the material system NiAl-34Cr is used. The chosen material and numerical parameters for the simulations are collected in Table A.4 and Table A.5, respectively. In this work, the same approximated thermodynamic energies as in [37] are used. The parameters are formulated in the notation presented in (4) and are summarized in Table A.6 in AppendixA. The setup used for the simulations is illustrated in Fig. 2. Similar to [49, 50], an infinite domain, perpendicular to the solidification front, is modeled by periodic boundary conditions. At the liquid end of the domain, a constant flux of melt into the domain is realized by the Dirichlet boundary condition. For the starting conditions, initially defined settings of lamellae pairs (lp), representing the phase fractions of the solid phases and labeled with Setting 1-6, are applied at the bottom of the domain ($x \leq 20$ voxel cells). The simulations of

the two-dimensional eutectic colony formation are performed with an initial setting of random seeds, using a Voronoi tessellation, as schematically illustrated with Setting V in Fig. 2. From the initial settings, the solid phases evolve in x -direction, with the velocity v_F . The growth direction and the velocity are controlled by the analytic temperature profile described in eq. (3) and shown in the lower part of Fig. 2.

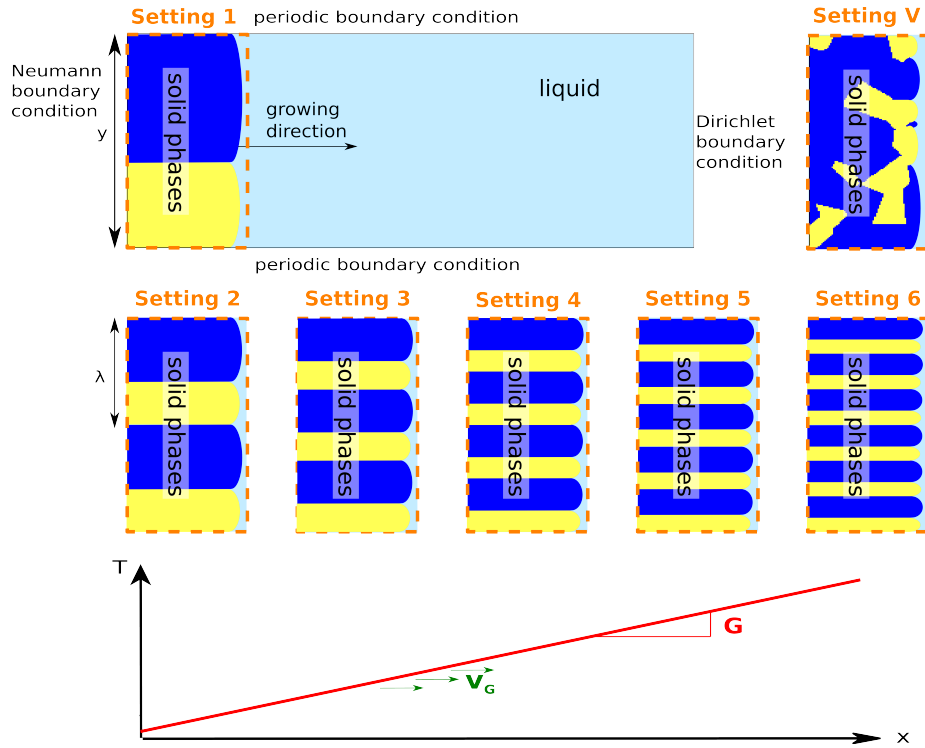


Figure 2: Applied two-dimensional simulation setups for the directional solidification of NiAl-34Cr.

For the validation of the nucleation mechanism, several simulations in different domain sizes are conducted for up to 10 million time steps (TS). While all simulations have the same height of 400 voxel cells in x -direction, the width of the domains in y -direction is varied from 36 up to 284 voxel cells. The large-scale simulations for the investigation of the eutectic colony formation are conducted

190 in a simulation domain of $1\,500 \times 10\,000$ voxel cells. Due to the use of a moving window technique [48, 51], the finally resulting structures reach after 20 million time steps a size of $25\,000 \times 10\,000$ voxel cells.

4. Results

For the two-dimensional simulation of eutectic colonies, the parameters of
195 the presented nucleation mechanism have to be adjusted to calibrate the growth conditions in the simulations. Therefore, a comparison between simulations with and without nucleation mechanism is conducted. The comparison is based on the relation of the undercooling ΔT , the growth velocity v and the spacing λ , as derived in [7], by Jackson and Hunt, for binary eutectic systems. Based on
200 these calibrations, large-scale simulations are subsequently performed in 2D, to investigate the influence of the applied temperature gradients on the formation of eutectic colonies.

4.1. Validation of the nucleation mechanism

The aim of the parameter calibration is an autonomous adjustment of the
205 lamellar spacing in the vicinity of λ_{ext} during the directional solidification of a two-phase eutectic system in two-dimensional simulations. The spacing λ_{ext} is related to the spacing with the maximum growth velocity for isothermal solidification and to the spacing of minimum undercooling for solidifications with temperature gradient [52]. Once the simulation has reached the vicinity of λ_{ext} , the
210 nucleation mechanism should not affect the relation between the undercooling ΔT , the growth velocity v and the spacing λ , as it is given by the corresponding simulations without nucleation mechanism. Therefore, a parameter set for the amplitude A and the intervention interval i from (5) as well as the limit for the concentration deviation c_{der} is derived for the system NiAl-34Cr, in order to
215 fulfill these constraints.

Derivation of the nucleation parameters. To adjust the limits for the concentration deviation, two simulation studies without the nucleation mechanism are

performed, using the initial Settings 1 and 2 from Fig. 2. The simulations are conducted with an isothermal temperature of ($T_4 = 0.993 \cdot T_{\text{eut}}$), to determine the spacing. For Setting 1, containing one pair of lamellae lp , the domain width y is varied from 36 to 126 cells and for Setting 2, containing two lp , the domain width y is varied from 72 to 144 cells. In all conducted simulations, the initial number of lamellae stays constant. For the two settings, the relation between the growth rate and the width of the simulation domain y is plotted in Fig. 3.

For the simulations with one pair of lamellae, λ_{ext} is found at 40 cells and for the simulations with two pairs of lamellae λ_{ext} is subsequent found at 80 cells. For a domain width y of $72 \leq y \leq 96$ cells, both settings lead to a stable growth without a change in the number of lamellae pairs. In this range, the growth velocity of the simulations with two lp is more than 12% higher than for the simulations with one lp . In the simulations starting from Setting 1, small oscillations of the phase widths occur in this range. Both observations indicate that the setting with two lamellae pairs leads to a higher stability of the growth for these domain widths. This assumption is also in accordance with the theory of Jackson and Hunt [7]. In a 2D simulation with only one pair of lamellae, the nucleation of a new phase would consequently result in a more stable lamellar spacing. To adjust the limits for the concentration deviation c_{der} of the nucleation mechanism, the concentration accumulations ahead of the solid phases are analyzed in the simulation with one lp and the domain width of 80 cells. In the lower part of Fig. 3 the averaged accumulations of Al, Cr and Ni in areas ahead of the solidification fronts are shown for the analyzed simulation.

From this, the limits of the deviations are extracted, which are required for the intervention of the nucleation mechanism. The derived limits are summarized in Table 1. The maximum deviation of c_{der} in fraction of the referring lever arm is 9.8% for the accumulation of Ni in front of the Cr-rich phase A2. To also enable a nucleation for domain widths, in which smaller amounts of accumulations form, the deviation limit is set to 8.5% in the following.

The parameters for the magnitude A of the noise function and its intervention interval i are derived on the basis of simulations with these concentration

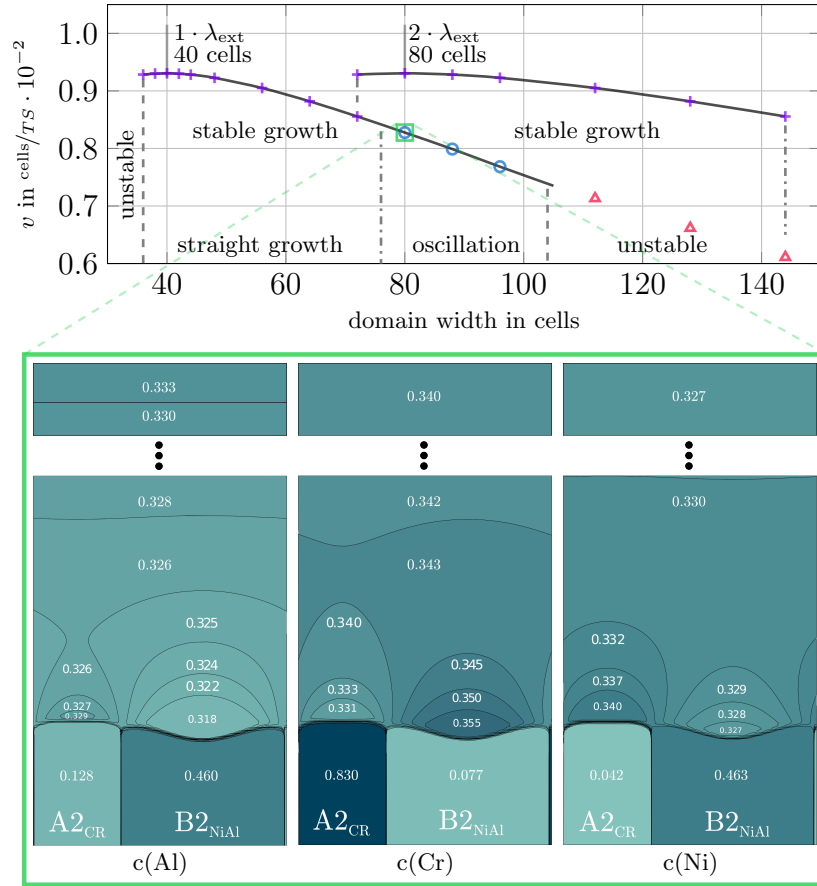


Figure 3: Plot of the velocity-spacing relationship for simulations with one and two set lamellae pairs. Violet crosses mark simulations with stable and straight growth, whereas simulations with oscillations are marked with blue circles. The red triangles indicate simulations in which one phase has been overgrown by the other. Below, concentration accumulations of Al, Cr and Ni ahead of the solidification front of a two-dimensional simulation of NiAl-34Cr using Setting 1 in a domain of 400×80 cells (green square in plot above) are shown.

Table 1: Summary of accumulations in front of the solidification front and derived concentration limits for the nucleation mechanism.

	<i>Al</i>	<i>Cr</i>	<i>Ni</i>
concentration in front of $A2_{Cr}$	0.329	0.331	0.340
c_{der} in front of $A2_{Cr}$	3.4 %	4.2 %	9.8 %
concentration in front of $B2_{NiAl}$	0.318	0.355	0.327
c_{der} in front of $B2_{NiAl}$	7.5 %	3.1 %	0.1 %
max c_{limit} for $c_{\text{der}} = 8.5 \%$	0.344	0.317	0.338
min c_{limit} for $c_{\text{der}} = 8.5 \%$	0.315	0.381	0.303

limits. These parameters are influenced by each other, as depending on the
250 height of the magnitude the diffusion in the system requires more iteration steps
to reduce the noise implemented disturbance. Too strong magnitudes and too
high rates lead to an unphysical escalation of the nucleation process, whereas,
too small values result in an unproductive mechanism. A promising combina-
tion of magnitude and interval is found for $A = 4$ and $i = 3000$. The following
255 studies, based on the theory of Jackson and Hunt, are performed with these
parameters.

Fig. 4 shows an exemplary simulation with the nucleation mechanism. Each
of the five intermediate states (a) to (e) shows the concentration field of Ni
with an adjusted color bar, to highlight the accumulations. Several nucleation
260 events of the NiAl-phase occur in the simulation. This leads to a competition
between the rods, resulting in overgrowing and merging events. During growth,
all microstructure events of nucleation, splitting, merging and overgrowing can
be observed in this simulation, as defined in [25]. Due to the nucleation of new
rods, the accumulations in the vicinity of the solidification front reduce from
265 (a) to (e). After the adjustment, the accumulations are less than the applied
concentration deviation criterion c_{der} and a stable growth of four rods occurs
(cf. (d) and (e)).

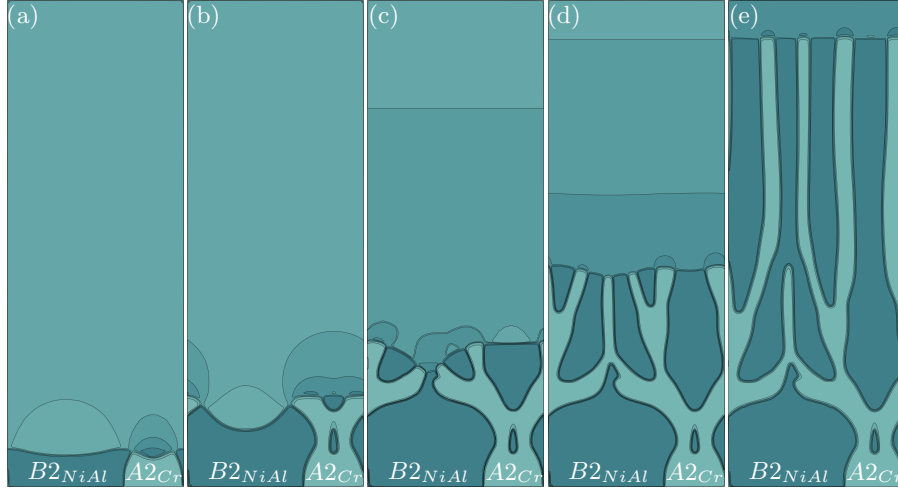


Figure 4: Illustration of a nucleation process for a two-dimensional simulation of NiAl-34Cr, in a domain of 400×180 cells, over five different time steps, labeled with (a) to (e). Starting from Setting 1 multiple splitting, nucleation, merging and overgrowing events lead to a stable growth of four lamellae pairs.

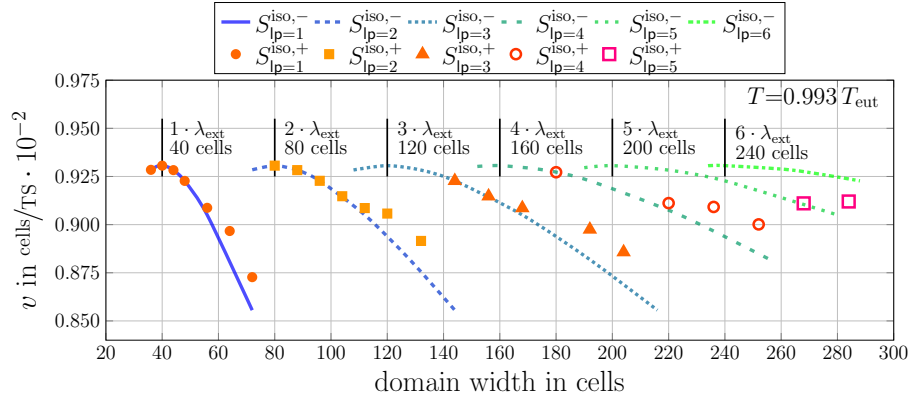
Jackson-Hunt studies with nucleation. To ensure that the evolving microstructure with nucleating rods is growing in the expected relationship between growth velocity, undercooling and spacing, two different simulation studies are conducted. In the first study, the velocity-spacing relationship is investigated for isothermal simulations S^{iso} with a temperature gradient G of zero and a temperature $T_{\text{sim}}^{\text{iso}}$ of 0.993, which corresponds to 1703 K. The temperature $T_{\text{sim}}^{\text{iso}}$ is non-dimensionalized with the eutectic temperature T_{eut} of 1715.08 K and represents 99.3% of T_{eut} . In the second study, the undercooling-spacing relationship for the simulations $S^{\nabla T}$ with the temperature gradient $G = 400 \text{ K/mm}$ and a constant gradient velocity v_G is analyzed. The velocity v_G is chosen similar to the solidification velocity of the isothermal simulations.

In both studies, simulations with and without the nucleation mechanism are performed, using different domain sizes. In addition to the tags \square^{iso} and $\square^{\nabla T}$ in the superscript for the temperature gradients, the tags \square^+ and \square^- are introduced to indicate simulations with and without the nucleation mechanism.

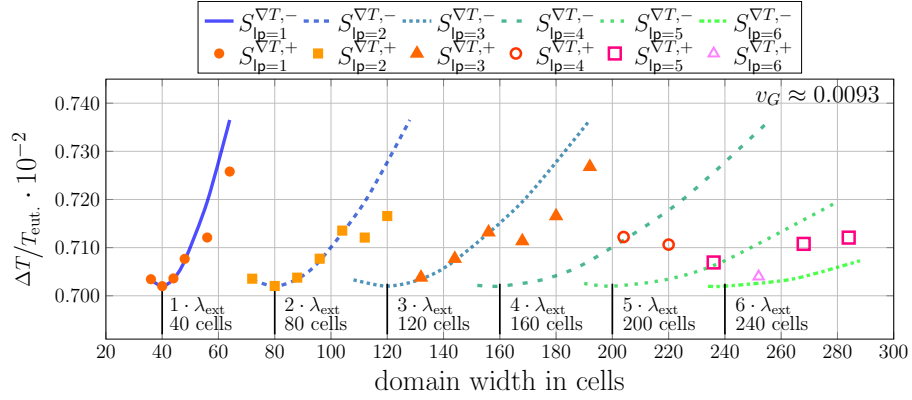
The simulations $S^{\text{iso},-}$ and $S^{\nabla T,-}$ are conducted as reference, using the initial start Settings 1 to 6 with different numbers of preset lamellae pairs, as illustrated in Fig. 2. All simulations with the nucleation mechanism start from Setting 1 with only one preset lamellae pair in the domain. For the velocity-spacing relationship, the results of the simulation studies are shown in Fig. 5(a) and for the undercooling-spacing relationship in Fig. 5(b). In all diagrams, the simulations $S^{\text{iso},-}$ and $S^{\nabla T,-}$ are plotted with lines, while the simulations $S^{\text{iso},+}$ and $S^{\nabla T,+}$ are plotted with different marks. The indices in the subscripts of the simulation labels, as well as the different marks, represent the final number of evolving lp after 10 million time steps.

As expected, the simulations without the nucleation mechanism show repeating sequences in both studies with extreme points at constant distances from each other. In Fig. 5(a) and in Fig. 5(b), all extreme points reach the same values for the velocity and the undercooling, respectively. Depending on the number of evolving lamellae pairs, the positions of the extreme points are located at an integer multiple of λ_{ext} . In the vicinity of λ_{ext} and $2 \cdot \lambda_{\text{ext}}$, the results of the simulations with the nucleation mechanism are in good accordance with the results of the reference simulations without nucleation. With an increasing distance from the extreme points, the reached velocities as well as undercoolings start to differ from the reference simulations. In these regions, the nucleation mechanism is already active, but it is either not strong enough or the conditions in the simulation are not benefiting enough for a successful nucleation. With a further increase of the domain width, the conditions become more favorable, until a new phase nucleates. After a stable phase has evolved, the values of the velocity and of the undercooling match with the reference curves for the next higher number of lamellae pairs.

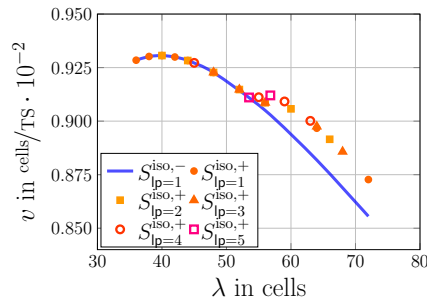
In Fig. 5(b), simulations with the temperature gradient $S^{\nabla T,+}$ already show successful nucleations for smaller domain sizes, in contrast to the isothermal simulations $S^{\text{iso},+}$ in Fig. 5(a). For domain widths larger than $3 \cdot \lambda_{\text{ext}}$, the number of evolving lamellae pairs is fluctuating. As shown in the plots, multiple settings of lamellae pairs can grow in a steady state for the same domain size. If a



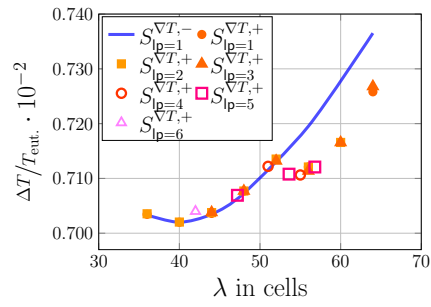
(a)



(b)



(c)



(d)

Figure 5: Comparison of the velocity-spacing relationship for isothermal simulations S^{iso} in (a) and the undercooling-spacing relationship for temperature-dependent simulations $S^{\nabla T}$ in (b) with + and without - the nucleation mechanism referred to the simulation domain. In (c) and (d), the relationships are referred to the the evolving lamellar spacing, respectively.

stable growth has established for a simulation with the nucleation mechanism,
315 the predefined conditions of the nucleation are no longer suitable to evolve
additional pairs of lamellae. This can lead in larger simulations to fewer pairs
of lamellae, compared to the corresponding reference simulations. Apart from
the domain size, the number of finally evolving lamellae pairs depend on the
growth history.

320 By referring the results from Fig. 5(a) and (b) to the finally evolving lamellar
spacing, the velocity-spacing relationship and the undercooling-spacing relation-
ship are replotted in Fig. 5(c) and (d), respectively. In a range from $0.9 \cdot \lambda_{\text{ext}}$
to $1.34 \cdot \lambda_{\text{ext}}$, the simulations with the nucleation mechanism are in good accor-
dance with the reference simulations. For evolved structures with larger lamellar
325 spacings, a deviation between the simulations with and without nucleation is
observed. As discussed before, the criterion for nucleation is already fulfilled in
these simulations and hence, the nucleus is not able to evolve. The maximum
deviation for both, velocity and undercooling, is less than 2% referred to the
reference simulations.

330 4.2. Investigation of eutectic colony formation

Based on the validated parameters for the nucleation mechanism, the growth
of eutectic colonies is investigated in two-dimensional phase-field simulations
in the following. To ensure a free growth of the microstructure, large-scale
two-dimensional domains of 1500×10000 cells are used. All simulations were
335 conducted on the SuperMUC system [53] on 1200 cores for ~ 100 h, to perform
20 million time steps. The finally evolved microstructure is shown in Fig. 6,
using the parameters from the previous validation.

The complete microstructure is shown in the middle of the image, surrounded
by enlargements of selected features labeled with (a) to (e), to illustrate differ-
ent effects during the evolution process. In Fig. 6(e) the formation of lamellae
340 from the initial Voronoi tessellation of Setting V is shown. Due to the used
parameter set from the Jackson-Hunt analysis, most of these lamellae evolve in
a straight growth, with an average lamellar spacing of 49.2 cells. This corre-

sponds to a $\sim 19\%$ larger lamellar spacing, compared to λ_{ext} from the simula-
 345 tions with small domain sizes. The spacings of the lamellae pairs vary in a range
 from 30 to 60 cells. Due to this variation of the lamellar spacing in the large-
 scale simulation and the concentration accumulation ahead of the solidification
 front, impurity-driven Mullins-Sekerka instabilities occur. These instabilities
 result in several microstructure adjustments of the lamellae during the growth.
 350 In Fig. 6(c) and (d), all microstructure events of nucleation, splitting, merging
 and overgrowing can be observed. In contrast to the previously shown sim-
 ulations in the small domains, mostly the Cr-rich fiber phase is nucleating in
 large domains during the microstructure evolution. In Fig. 6(b), a competition
 between two evolving lamellar structures is depicted. Many competition areas
 355 can be found in Fig. 6(a), showing the solidification front after 20 million time
 steps. The structures between these areas form one eutectic colony.

For a better investigation of the colony formation and interaction, the num-
 ber of colonies in one simulation has to be increased. Therefore, either the
 domain size needs to be increased or the instabilities have to be enhanced. To
 360 keep the computational effort in a reasonable range, the colony formation is
 promoted by decreasing the intervention interval i and the concentration devi-
 ation c_{der} to 1000 and 4%, respectively. As a result, the growth velocity of the
 isothermal simulation is increased by 7.0%.

To systematically investigate the colony formation for comparable structures,
 365 2D large-scale simulations with different temperature gradients are performed,
 as given in Table 2, together with their physical expressions.

Table 2: Summary of the applied temperature gradients together with their physical units.

		G_0	G_{20}	G_{40}	G_{100}	G_{400}
∇T	$T_{\text{sim}}/\text{cells}$	0	$1.76 \cdot 10^{-7}$	$3.51 \cdot 10^{-7}$	$8.78 \cdot 10^{-7}$	$3.51 \cdot 10^{-6}$
	K/mm	0	20	40	100	400

In Fig. 7, the solidification fronts from the simulations with different applied

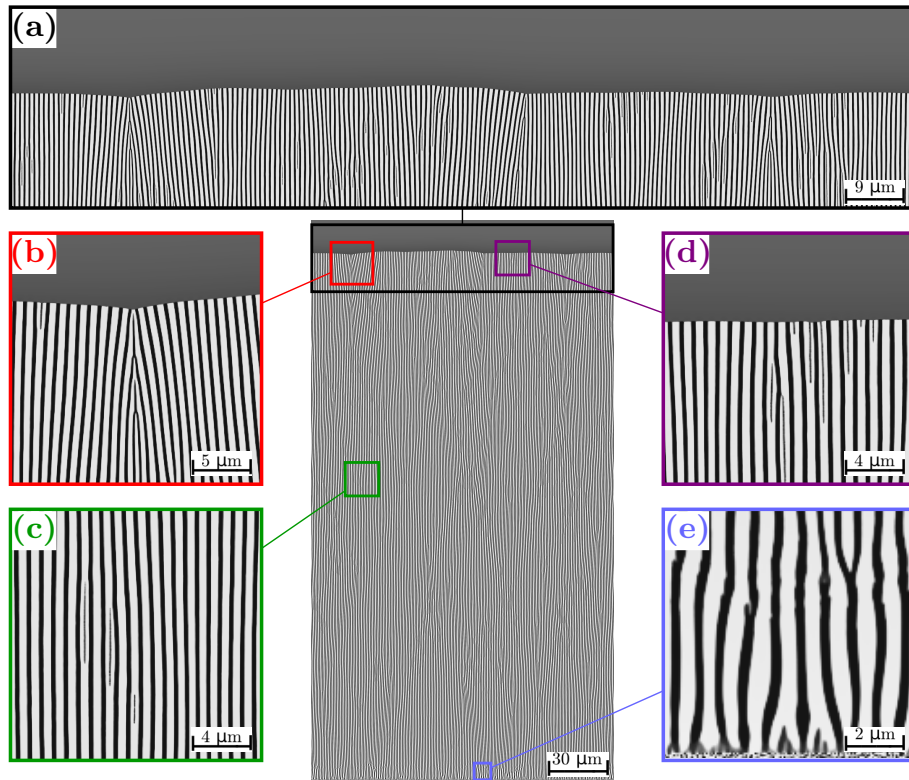


Figure 6: Resulting microstructure of an isothermal 2D large-scale simulation of NiAl-34Cr, surrounded by enlargements of the selected features labeled with (a) to (e). For the nucleation mechanism, an amplitude A of 4, an intervention interval i of 3000 and a limit for the concentration deviation c_{der} of 8.5% is used.

Table 3: Analysis of colony widths, heights and lamellar spacings after 20 million time steps depending on the applied nucleation parameters and temperature gradients.

i	$c_{\text{der}}[\%]$	∇T [K/mm]	λ_{rods} [cells]	λ_{colony} [cells]	h_{colony} [cells]
3000	8.5	0	49.2 ± 19.2	3333 ± 1074	72.5 ± 65
1000	4	0	47.5 ± 20.9	1667 ± 1358	224.2 ± 190
1000	4	20	47.8 ± 39.5	1667 ± 653	218.2 ± 108
1000	4	40	45.1 ± 25.2	1667 ± 716	203.8 ± 99
1000	4	100	46.5 ± 25.2	1667 ± 821	169.6 ± 68
1000	4	400	44.4 ± 25.8	1667 ± 1002	51.7 ± 23

temperature gradients are shown after 20 million time steps. For all simulations, the solidification velocities converge to a similar value, as depicted in the velocity plot in the lower part of the figure. In contrast to the simulation shown in Fig. 6, multiple well-pronounced colonies with convex solidification fronts evolve for the simulations with modified parameters. In general, the rods in the middle of a colony mainly show straight growth. In the vicinity of the contact areas between two colonies, the rod growth is no longer directed in the direction of the applied temperature gradient, which results in a curved growth with multiple splitting and nucleation events. As expected, the height difference at the solidification front decreases with an increasing temperature gradient. However, independent from the temperature gradient, all solidification fronts consist of six colonies after simulating 20 million time steps. For the temperature gradient of zero, it can be assumed that the smallest colony is overgrown by further solidification. Quantitative analyzes of the visually described trends for the colony widths λ_{colony} , the heights h_{colony} and the rod spacing λ_{rod} are compiled in Table 3.

As an example, the simulation with an applied temperature gradient of 20 K/mm is discussed in more detail. The fully evolved microstructure after 20 million time steps as well as enlargements of the selected microstructure features of this simulation are shown in Fig. 8. For the other simulations, similar

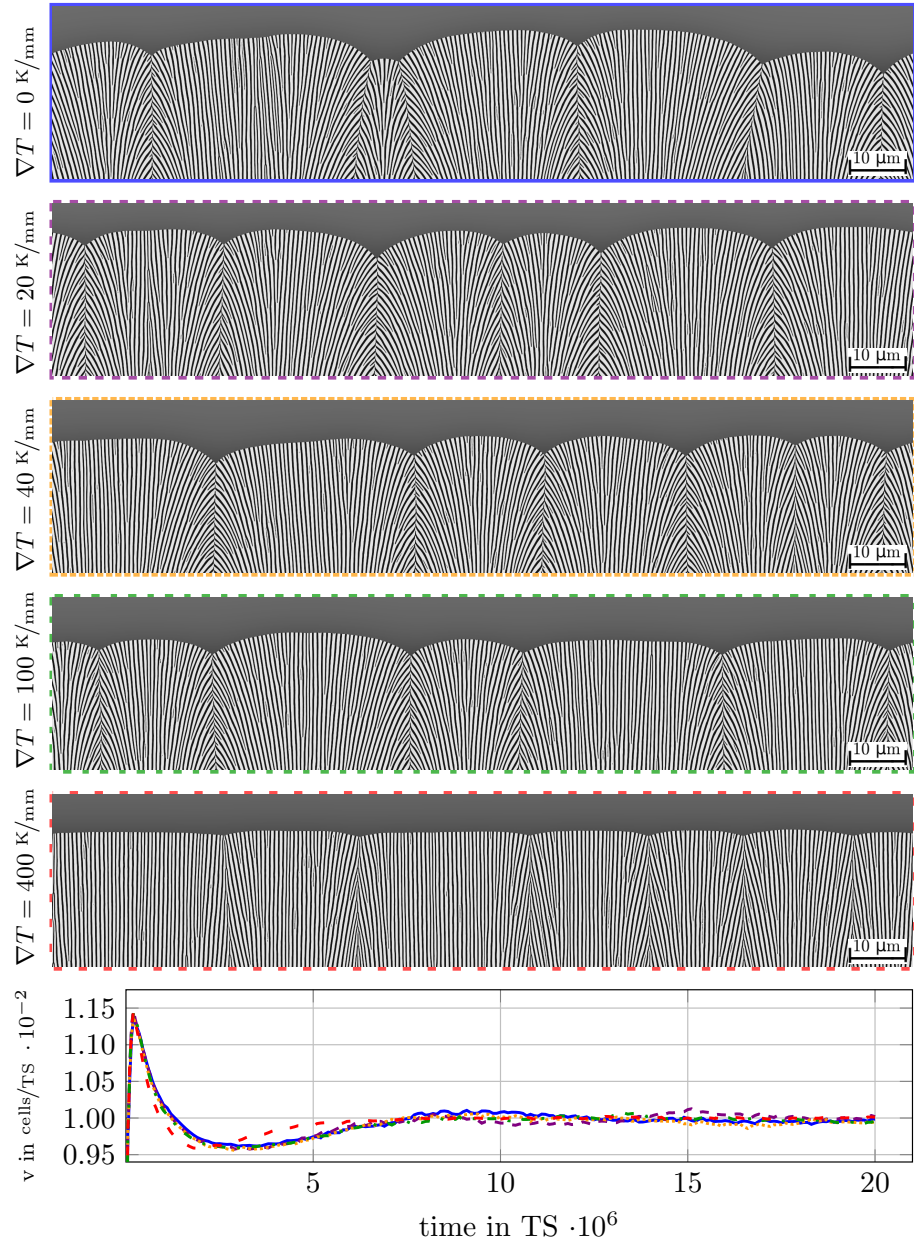


Figure 7: Comparison of solidification fronts after 20 million time steps for the simulations with different temperature gradients. The diagram displays the corresponding velocity profiles over the simulation time.

illustrations are depicted in the Figs. B.10 to B.13 in AppendixB. In Fig. 8(a), the evolved solidification front with multiple colonies is highlighted, while in (b) the straight growth of a colony is shown. Similar to the adjustments of the rods in classical eutectic solidification [25], microstructure events can be found during the evolution of eutectic colonies. In Fig. 8(c), the overgrowth of two colonies is depicted. In contrast to the events of rods, an overgrowth of a colony in 2D is not combined with a merging event. The overgrowing colonies are just forming a new contact area, instead of combining to one colony. The formation of a new colony is indicated in Fig. 8(d).

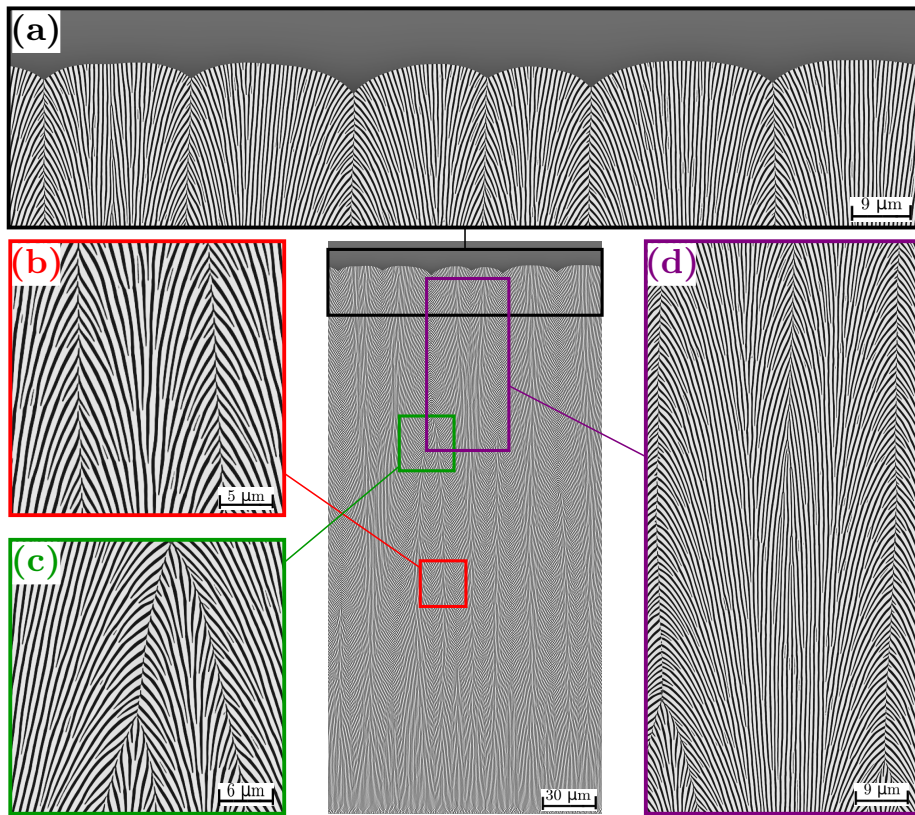


Figure 8: Resulting microstructure of a 2D large-scale simulation of NiAl-34Cr with an applied temperature gradient of 20 K/mm, surrounded by the enlargements of selected features, which are labeled with (a) to (d). For the nucleation mechanism, an amplitude A of 4, an intervention interval i of 1000 and a limit of 4%, for the concentration deviation c_{der} , is used.

To highlight the formation process in more detail, the evolution of the microstructure in the enlarged section of Fig. 8(d) is shown in Fig. 9 for six different time steps, labeled with (a) to (f). On both sides of this section, one colony is overgrown during the first two time steps, shown in (a) and (b). Hence, the width of the colony in the center is increasing. During the enlargement of this colony, a concave shape occurs in the middle of the overall convex solidification front between the time steps depicted in (c) and (d). This behavior is comparable to an enlarged rod before nucleation, as exemplarily shown in Fig. 4. For the whole colony, a kind of double peak profile establishes. In contrast to the 2D formation of new rods, a new contact area between colonies is forming in the middle of the double peak profile, instead of a nucleation event. This leads to a division of the original colony into two colonies.

The division of colonies is observed in all simulations with a temperature gradient between 0 and 40 K/mm . The sizes of the colonies, at which the division occurs, is decreasing with increasing temperature gradients. In the isothermal simulation, the division occurs at a colony spacing of ~ 3228 cells, whereas in the simulation with a temperature gradient of 20 and 40 K/mm it occurs at a spacing of ~ 2624 and ~ 2092 cells, respectively. All divisions occur at a height-to-length ratio of 0.115, which is $\sim 10\%$ smaller than the average ratio in the simulations.

Depending on the material system and the process conditions, different morphologies of the colonies are reported from experiments and simulations [8–10, 13, 54]. The presented colonies in this work are composed of multiple lamellae pairs, which is in contrast to the colonies presented in the experimental work of Hecht et al. [10] and in the simulative works of Plapp and Karma [13], as well as of Lahiri et al. [54]. In the presented simulations, no penetration of the liquid phase between the colonies is observed. The number of rods in the presented colonies is comparable to reported experimental results of Raj and Locci for the related system Ni-Al-Cr-Mo in [8] and of Durand-Charre and Durand for the systems MnSb-(Sb,Bi) and MnSb-(Sb,Sn) in [9].

Based on the good qualitative accordance of the presented simulations, the

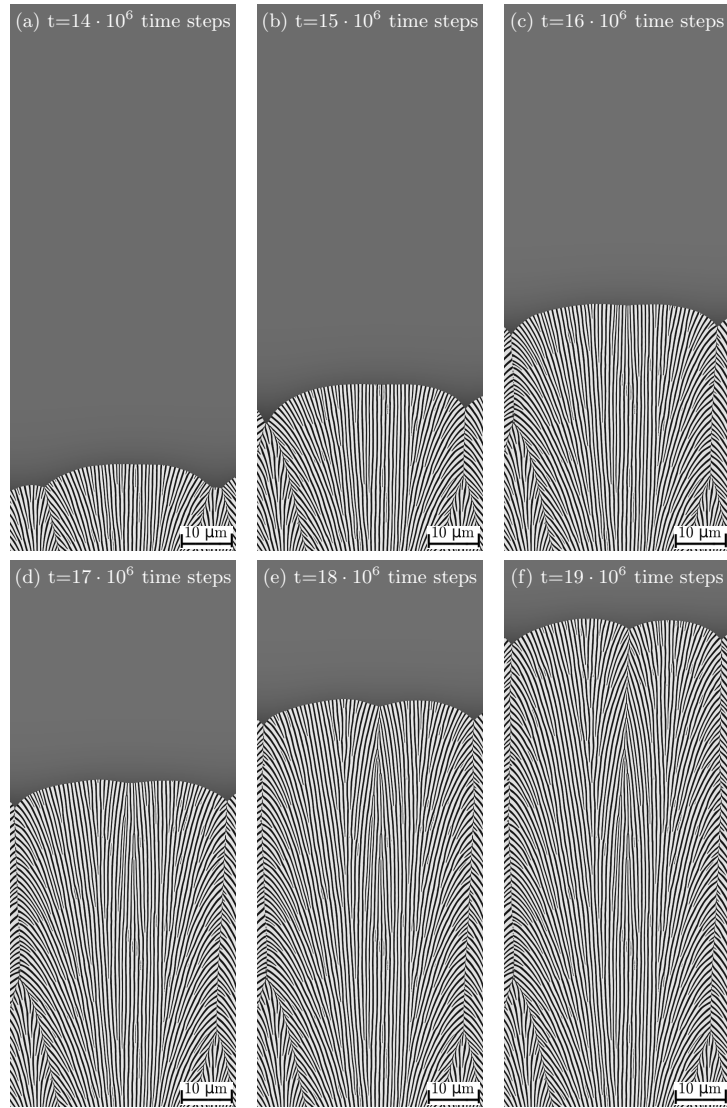


Figure 9: Transformation process from one to two colonies over six different time steps (a) to (f).

used phase-field and material models are suitable for the investigation of eutectic colony formations. For a further validation of the models, more studies with different process conditions as well as a comparison with experimental results
430 are required.

5. Conclusion

The aim of this work is to investigate the formation process of multiple eutectic colonies in two dimensional phase-field simulations. Therefore, a concentration-driven nucleation mechanism is derived in the context of a multiphase-field
435 framework, to ensure a free growth of multiple lamellae pairs. The nucleation mechanism is adjusted and validated by comparing simulations with and without a nucleation mechanism with the theory of Jackson and Hunt for lamellar growth. On this basis, the formation of eutectic colonies and their interaction are investigated in two-dimensional large-scale phase-field simulations de-
440 pending on the applied temperature gradient. From the simulation results, the following observations and conclusions are made:

- (i) For simulations with and without the nucleation mechanism, a good accordance is found in the vicinity of λ_{ext} for the velocity-spacing as well as for the undercooling-spacing relationship. Hence, the derived and ad-
445 justed nucleation method is able to efficiently simulate the formation of multiple eutectic colonies in large-scale 2D domains.
- (ii) For domain sizes larger than three times λ_{ext} , several stable settings with different numbers of lamellae pairs are found. From this, it can be concluded that the final number of evolving lamellae pairs is affected by the
450 domain size and by the growth history of the microstructure.
- (iii) In large-scale 2D simulations, the simultaneous formation process of multiple eutectic colonies is observed by applying the derived nucleation method.
- (iv) The applied temperature gradients affects the height of the colonies and the spacing of the rods, but not the number of the evolving colonies.

455 (v) Within the colonies, multiple splitting, merging, nucleation and overgrowing events of the rods occur as a reaction of the concentration accumulations.

(vi) Similar to the evolution of eutectic structures, rearrangement events are observed for the multiple times larger colonies. An increase of the colony number is achieved by a division of a large colony into two colonies by
460 forming a new contact area. A decrease is achieved through an overgrowth of a colony by its neighbors.

The effect of velocity variations on the colony formation is of high interest for future works. Furthermore, due to the computational resources required
465 to capture the different length scales between the rods and the colonies, the formation process in three dimensions remains an open topic.

6. Acknowledgment

We are grateful for the provided computational resources at the Leibniz Rechenzentrum in Munich and thank Marco Seiz and Leon Geisen for the helpful
470 discussions and their support. We also thank Prof. Dr. Mathis Plapp from Ecole Polytechnique for the fruitful discussions on the analysis of the colony structures. Furthermore, the authors are grateful for the financial support within the project SKAMPY (Ultra-scalable multiphysics simulations for solidification processes in metals) funded by BMBF, the cooperative graduate school “Gefügeanalyse und
475 Prozessbewertung” of the Ministry of Baden-Württemberg and the Helmholtz graduate school “Integrated Materials Development for Novel High Temperature Alloys”.

Appendix A. Parameter sets for simulations

Table A.4: Summary of material parameters in dimensionless simulation units and their physical units.

parameter	simulation value	physical value
D	2.5	$1.25 \cdot 10^{-9} \text{ m}^2/\text{s}$
γ	phase $A2$ $B2$ ℓ $A2$ $B2$ ℓ	$\begin{bmatrix} - & \gamma_{\alpha\beta} & \gamma_{\alpha\ell} \\ \gamma_{\beta\alpha} & - & \gamma_{\beta\ell} \\ \gamma_{\ell\alpha} & \gamma_{\ell\beta} & - \end{bmatrix}$
$\gamma_{\alpha\beta}, \gamma_{\beta\alpha}$	0.013	2.0 J/m^2
$\gamma_{\alpha\ell}, \gamma_{\ell\alpha}$	0.016	2.5 J/m^2
$\gamma_{\beta\ell}, \gamma_{\ell\beta}$	0.013	2.0 J/m^2
$\gamma_{\alpha\beta\delta}$	0.208	
phase fraction of $A2, B2$	$0.\bar{3}, 0.\bar{6}$	

Table A.5: Summary of material parameters in dimensionless simulation units and their physical units.

parameter	simulation value	physical value
Δx	1.0	$1.5 \cdot 10^{-8}$ m
ϵ	5.0	$7.5 \cdot 10^{-8}$ m
Δt	0.1	$4.5 \cdot 10^{-8}$ s
$\boldsymbol{\tau}$	phase	$A2 \quad B2 \quad \ell$
	$A2$	$\left[\begin{array}{ccc} - & \tau_{\alpha\beta} & \tau_{\alpha\ell} \end{array} \right]$
	$B2$	$\left[\begin{array}{ccc} \tau_{\beta\alpha} & - & \tau_{\beta\ell} \end{array} \right]$
	ℓ	$\left[\begin{array}{ccc} \tau_{\ell\alpha} & \tau_{\ell\beta} & - \end{array} \right]$
$\tau_{\alpha\beta}, \tau_{\beta\alpha}$	0.52705	
$\tau_{\alpha\ell}, \tau_{\ell\alpha}$	0.23877	based on [40]
$\tau_{\beta\ell}, \tau_{\ell\beta}$	0.39319	

Table A.6: Fitted thermodynamic energies from the CALPHAD-database of Peng et al. [41] written as dimensionless simulation parameters in matrix notation and their values in physical units. The parameters are similar to the energies used in [37].

phase	parameter	simulation value	physical value
Cr-rich A2	$\mathbf{\Xi}_{A2}$	$\begin{bmatrix} 3.29 & 1.75 \\ 1.75 & 1.54 \end{bmatrix}$	$\begin{bmatrix} 329282 & 175062 \\ 175062 & 154856 \end{bmatrix} \text{ J/mol}$
	ξ_{A2}	$\begin{bmatrix} -3.80 \\ -2.42 \end{bmatrix}$	$\begin{bmatrix} -379838 \\ -242302 \end{bmatrix} \text{ J/mol}$
	X_{A2}	0.03	-3257 J/mol
NiAl-rich B2	$\mathbf{\Xi}_{B2}$	$\begin{bmatrix} 3.88 & 1.96 \\ 1.96 & 1.90 \end{bmatrix}$	$\begin{bmatrix} 387820 & 195574 \\ 195574 & 189791 \end{bmatrix} \text{ J/mol}$
	ξ_{B2}	$\begin{bmatrix} -4.01 \\ -1.50 \end{bmatrix}$	$\begin{bmatrix} -401248 \\ -149767 \end{bmatrix} \text{ J/mol}$
	X_{B2}	-0.48	-48777 J/mol
liquid	$\mathbf{\Xi}_\ell$	$\begin{bmatrix} 1.80 & 0.82 \\ 0.82 & 0.58 \end{bmatrix}$	$\begin{bmatrix} 180047 & 82296 \\ 82296 & 57830 \end{bmatrix} \text{ J/mol}$
	ξ_ℓ	$\begin{bmatrix} -1.81 \\ -0.34 \end{bmatrix}$	$\begin{bmatrix} 181003 \\ 34700 \end{bmatrix} \text{ J/mol}$
	X_ℓ	$-0.25 - 0.75 \cdot T$	$-25133 \text{ J/mol} - 44.166 \cdot T \text{ J/mol K}$

Appendix B. Colony formation depending on the temperature gradient in NiAl-34Cr

480

Similar to the discussed microstructure in Fig. 8, the simulation results for colonies with the temperature gradients G_0 , G_{40} , G_{100} and G_{400} are shown in Figs. B.10 to B.13. In (a) the solidification front after 20 million time steps is enlarged. Depending on the growth history, different features like the straight
485 evolution of contact areas between two colonies, the overgrowth of a colony and the division of one large colony into two smaller ones are highlighted in the different enlargements (b) to (e) or (b) to (d), respectively.

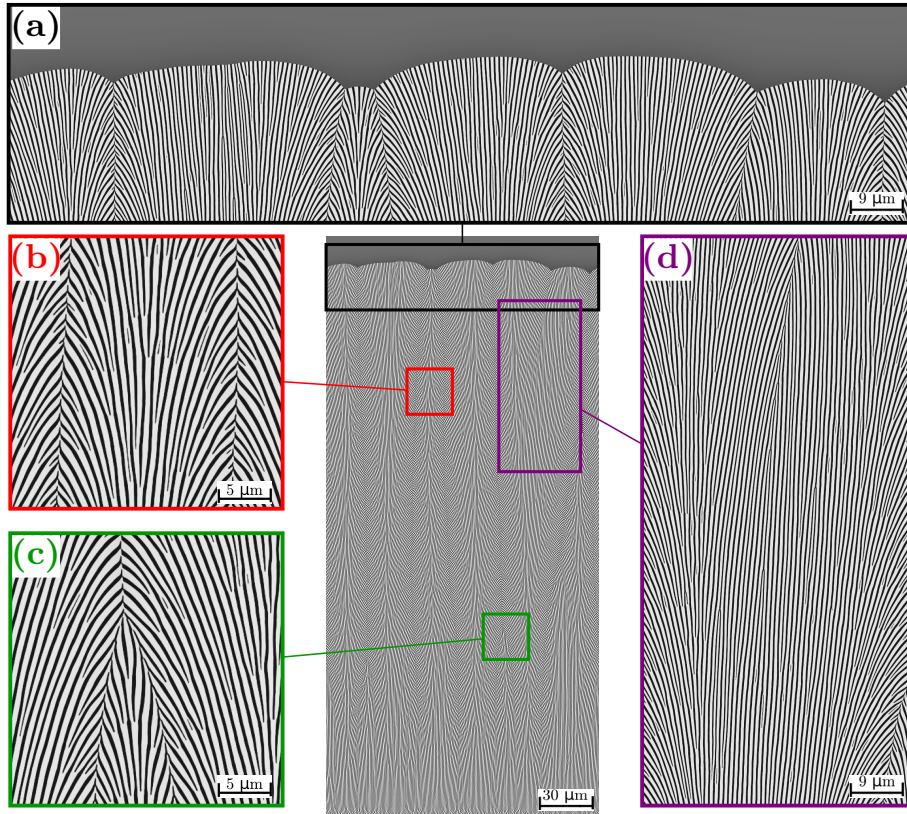


Figure B.10: Resulting microstructure of an isothermal 2D large-scale simulation of NiAl-34Cr surrounded by enlargements of the selected features labeled with (a) to (d). For the nucleation mechanism, an amplitude A of 4, an intervention interval i of 1000 and a limit of 4%, for the concentration deviation c_{der} , is used.

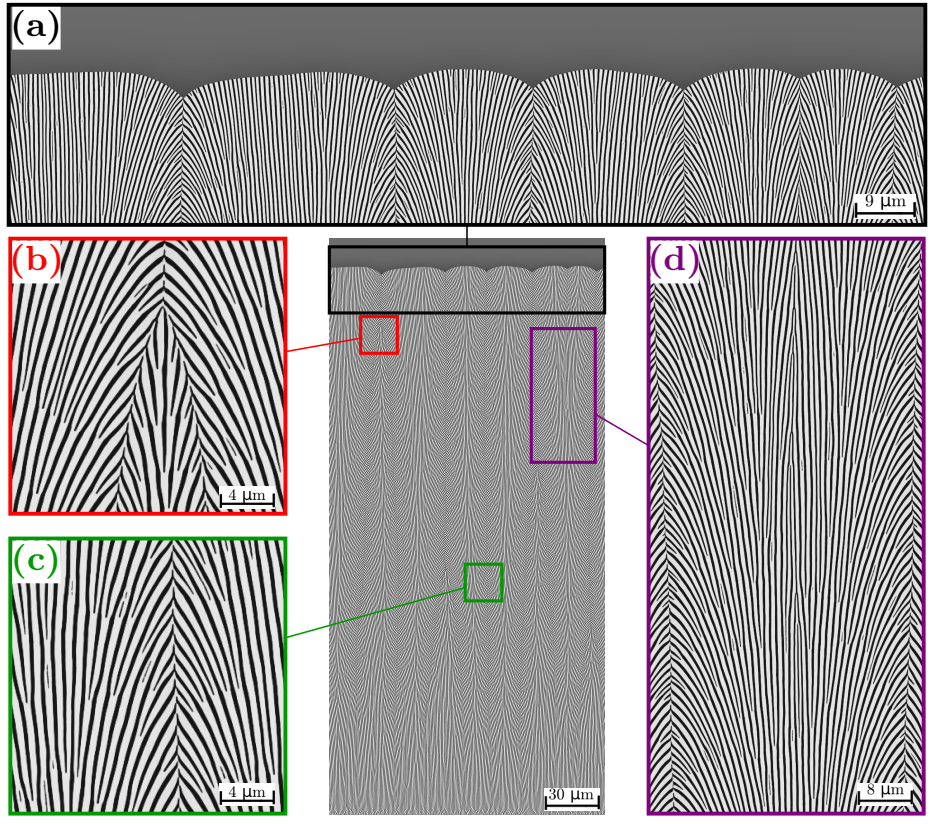


Figure B.11: Resulting microstructure of a 2D large-scale simulation of NiAl-34Cr with an applied temperature gradient of 40 K/mm surrounded by enlargements of the selected features, labeled with (a) to (d). For the nucleation mechanism, an amplitude A of 4, an intervention interval i of 1000 and a limit of 4%, for the concentration deviation c_{der} , is used.

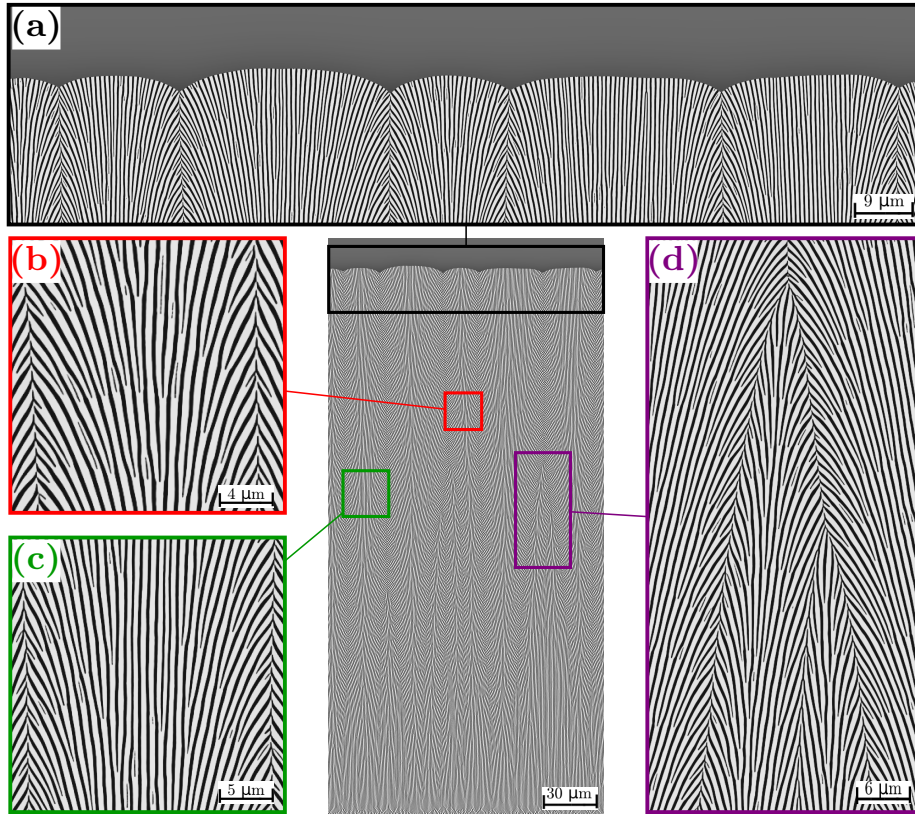


Figure B.12: Resulting microstructure of a 2D large-scale simulation of NiAl-34Cr with an applied temperature gradient of 100 K/mm surrounded by enlargements of the selected features, labeled with (a) to (d). For the nucleation mechanism, an amplitude A of 4, an intervention interval i of 1000 and a limit of 4%, for the concentration deviation c_{der} , is used.

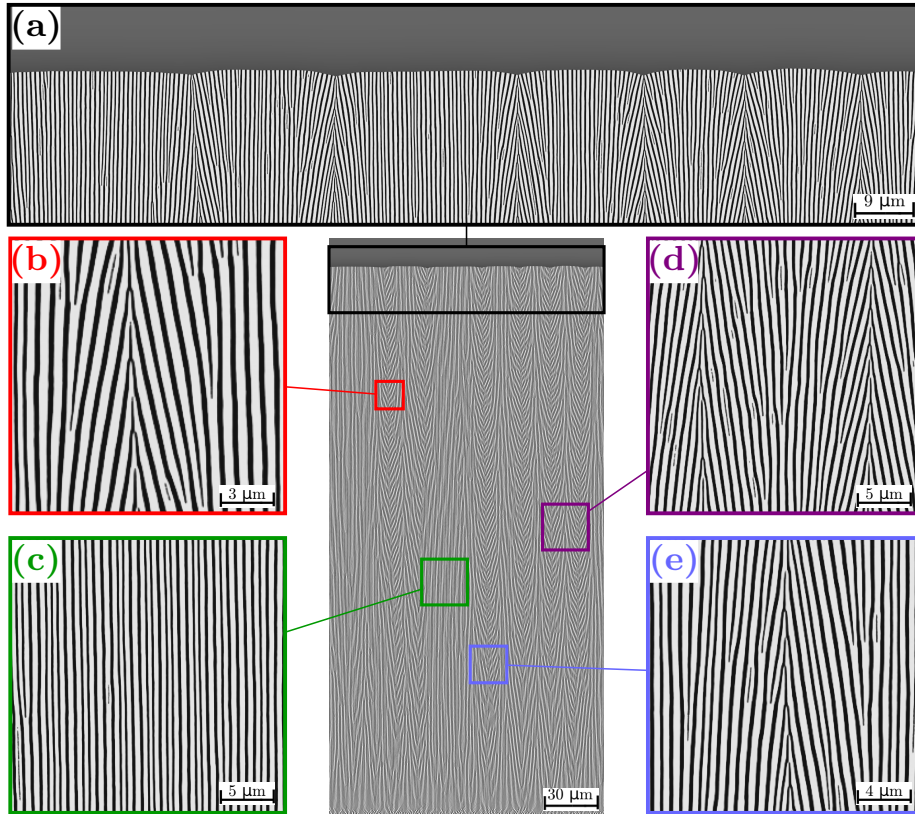


Figure B.13: Resulting microstructure of a 2D large-scale simulation of NiAl-34Cr with an applied temperature gradient of 400 K/mm surrounded by enlargements of the selected features, labeled with (a) to (e). For the nucleation mechanism, an amplitude A of 4, an intervention interval i of 1000 and a limit of 4%, for the concentration deviation c_{der} , is used.

References

- [1] M. Rinaldi, R. Sharp, M. Flemings, Growth of ternary composites from
490 the melt: Part II, *Metallurgical Transactions* 3 (1972) 3139–3148.
- [2] S. Akamatsu, G. Faivre, Traveling waves, two-phase fingers, and eutectic
colonies in thin-sample directional solidification of a ternary eutectic alloy,
Physical Review E 61 (2000) 3757.
- [3] W. W. Mullins, R. F. Sekerka, Morphological stability of a particle growing
495 by diffusion or heat flow, *Journal of applied physics* 34 (1963) 323–329.
- [4] W. W. Mullins, R. F. Sekerka, Stability of a planar interface during so-
lidification of a dilute binary alloy, *Journal of applied physics* 35 (1964)
444–451.
- [5] R. Sekerka, A stability function for explicit evaluation of the mullins-
500 sekerka interface stability criterion, *Journal of Applied Physics* 36 (1965)
264–268.
- [6] R. Sekerka, Morphological stability, *Journal of Crystal Growth* 3 (1968)
71–81.
- [7] K. A. Jackson, J. D. Hunt, Lamellar and rod eutectic growth, *Transactions*
505 *of the Metallurgical Society of AIME* 236 (1966) 1129–1142.
- [8] S. Raj, I. Locci, Microstructural characterization of a directionally-
solidified ni-33 (at.%) Al-31Cr-3Mo eutectic alloy as a function of with-
drawal rate, *Intermetallics* 9 (2001) 217–227.
- [9] M. Durand-Charre, F. Durand, Effects of growth rate on the morphology
510 of monovariant eutectics: MnSb–(Sb, Bi) and MnSb–(Sb, Sn), *Journal of*
Crystal Growth 13 (1972) 747–750.
- [10] U. Hecht, V. Witusiewicz, A. Drevermann, Coupled growth of Al-Al₂Cu
eutectics in Al–Cu–Ag alloys, *IOP Conference Series: Materials Science*
and Engineering 27 (2012) 012029.

- 515 [11] T. Himemiya, Growth models of two-phase eutectic cell in a ternary eutectic system: a phase selection map, *Materials Transactions, JIM* 40 (1999) 675–684.
- [12] M. Plapp, A. Karma, Eutectic colony formation: A stability analysis, *Physical Review E* 60 (1999) 6865.
- 520 [13] M. Plapp, A. Karma, Eutectic colony formation: A phase-field study, *Physical Review E* 66 (2002) 061608.
- [14] A. Lahiri, A. Choudhury, Effect of Surface Energy Anisotropy on the Stability of Growth Fronts in Multiphase Alloys, *Transactions of the Indian Institute of Metals* 68 (2015) 1053–1057.
- 525 [15] C. Lan, Y. Chang, Efficient adaptive phase field simulation of directional solidification of a binary alloy, *Journal of Crystal Growth* 250 (2003) 525–537.
- [16] C. Lan, C. Shih, W. Hsu, Long-time scale morphological dynamics near the onset of instability during directional solidification of an alloy, *Journal of crystal growth* 264 (2004) 379–384.
- 530 [17] C. Lan, C. Shih, M. Lee, Quantitative phase field simulation of deep cells in directional solidification of an alloy, *Acta materialia* 53 (2005) 2285–2294.
- [18] C. Lan, M. Lee, M. Chuang, C. Shih, Phase field modeling of convective and morphological instability during directional solidification of an alloy, *Journal of crystal growth* 295 (2006) 202–208.
- 535 [19] T. Pusztai, L. Rátkai, A. Szállás, L. Gránásy, Spiraling eutectic dendrites, *Physical Review E* 87 (2013) 032401.
- [20] L. Rátkai, A. Szállás, T. Pusztai, T. Mohri, L. Gránásy, Ternary eutectic dendrites: Pattern formation and scaling properties, *The Journal of chemical physics* 142 (2015) 154501.
- 540

- [21] S. Akamatsu, M. Perrut, S. Bottin-Rousseau, G. Faivre, Spiral two-phase dendrites, *Physical Review Letters* 104 (2010) 056101.
- [22] S. Akamatsu, S. Bottin-Rousseau, G. Faivre, E. A. Brener, Scaling theory of two-phase dendritic growth in undercooled ternary melts, *Physical review letters* 112 (2014) 105502.
- 545
- [23] A. Karma, M. Plapp, New insights into the morphological stability of eutectic and peritectic coupled growth, *JOM* 56 (2004) 28–32.
- [24] J. Hötzer, M. Jainta, P. Steinmetz, B. Nestler, A. Dennstedt, A. Genau, M. Bauer, H. Köstler, U. Råde, Large scale phase-field simulations of directional ternary eutectic solidification, *Acta Materialia* 93 (2015) 194–204.
- 550
- [25] P. Steinmetz, J. Hötzer, A. Dennstedt, C. Serr, B. Nestler, A. Genau, Graph-based investigation of three-dimensional microstructure rearrangement during ternary eutectic directional solidification of al-ag-cu, *Journal of Crystal Growth* 498 (2018) 230–243.
- 555
- [26] T. W. Heo, L.-Q. Chen, Phase-field modeling of nucleation in solid-state phase transformations, *Jom* 66 (2014) 1520–1528.
- [27] B. Böttger, J. Eiken, I. Steinbach, Phase field simulation of equiaxed solidification in technical alloys, *Acta materialia* 54 (2006) 2697–2704.
- [28] E. Schoof, D. Schneider, N. Streichhan, T. Mittnacht, M. Selzer, B. Nestler, Multiphase-field modeling of martensitic phase transformation in a dual-phase microstructure, *International Journal of Solids and Structures* 134 (2018) 181–194.
- 560
- [29] B. Nestler, A. Wheeler, A multi-phase-field model of eutectic and peritectic alloys: numerical simulation of growth structures, *Physica D: Nonlinear Phenomena* 138 (2000) 114–133.
- 565

- [30] F. Podmaniczky, G. I. Tóth, T. Pusztai, L. Gránásy, Investigating nucleation using the phase-field method, *Journal of the Indian Institute of Science* 96 (2016) 161–177.
- 570 [31] D. Miracle, Overview no. 104 the physical and mechanical properties of NiAl, *Acta Metallurgica et Materialia* 41 (1993) 649–684.
- [32] R. Darolia, Structural applications of NiAl, *Journal of Material Science and Technology* 10 (1994) 157–169.
- [33] R. D. Noebe, R. R. Bowman, M. V. Nathal, Review of the physical and
575 mechanical properties and potential applications of the B2 compound NiAl, NASA Technical Memorandum 105598 (1992).
- [34] G. Frommeyer, R. Rablbauer, H. Schäfer, Elastic properties of B2-ordered NiAl and NiAl–X (Cr, Mo, W) alloys, *Intermetallics* 18 (2010) 299–305.
- [35] J. L. Walter, H. E. Cline, The effect of solidification rate on structure
580 and high-temperature strength of the eutectic NiAl–Cr, *Metallurgical and Materials Transactions B* 1 (1970) 1221–1229.
- [36] S. M. Merchant, M. R. Notis, A review: Constitution of the Al–Ni–Cr system, *Materials Science and Engineering* 66 (1984) 47–60.
- [37] M. Kellner, I. Sprenger, P. Steinmetz, J. Hötzer, B. Nestler, M. Heilmaier,
585 Phase-field simulation of the microstructure evolution in the eutectic NiAl–34Cr system, *Computational Materials Science* 128 (2017) 379–387.
- [38] M. Kellner, W. Kunz, P. Steinmetz, J. Hötzer, B. Nestler, Phase-field study of dynamic velocity variations during directional solidification of eutectic NiAl–34Cr, *Computational Materials Science* 145 (2018) 291 – 305.
- 590 [39] M. Plapp, Unified derivation of phase-field models for alloy solidification from a grand-potential functional, *Physical Review E* 84 (2011) 031601.

- [40] A. Choudhury, B. Nestler, Grand-potential formulation for multicomponent phase transformations combined with thin-interface asymptotics of the double-obstacle potential, *Physical Review E* 85 (2012) 021602.
- 595 [41] J. Peng, P. Franke, H. J. Seifert, Experimental investigation and calphad assessment of the eutectic trough in the system NiAl-Cr-Mo, *Journal of Phase Equilibria and Diffusion* 37 (2016) 592–600.
- [42] A. Choudhury, M. Kellner, B. Nestler, A method for coupling the phase-field model based on a grand-potential formalism to thermodynamic databases, *Current Opinion in Solid State and Materials Science* 19 (2015) 287–300.
- 600 [43] B. Nestler, H. Garcke, B. Stinner, Multicomponent alloy solidification: Phase-field modeling and simulations, *Phys. Rev. E* 71 (2005) 041609.
- [44] A. Karma, Phase-field formulation for quantitative modeling of alloy solidification, *Physical Review Letters* 87 (2001) 115701.
- 605 [45] B. Echebarria, R. Folch, A. Karma, M. Plapp, Quantitative phase-field model of alloy solidification, *Physical Review E* 70 (2004) 061604.
- [46] N. Moelans, A quantitative and thermodynamically consistent phase-field interpolation function for multi-phase systems, *Acta Materialia* 59 (2011) 1077–1086.
- 610 [47] J. Hötzer, O. Tschukin, M. B. Said, M. Berghoff, M. Jainta, G. Barthelemy, N. Smorchkov, D. Schneider, M. Selzer, B. Nestler, Calibration of a multiphase field model with quantitative angle measurement, *Journal of Materials Science* 51 (2015) 1788–1797.
- 615 [48] J. Hötzer, A. Reiter, H. Hierl, P. Steinmetz, M. Selzer, B. Nestler, The parallel multi-physics phase-field framework Pace3D, *Journal of Computational Science* 26 (2018) 1 – 12.

- [49] K. D. Noubary, M. Kellner, P. Steinmetz, J. Hötzer, B. Nestler, Phase-field study on the effects of process and material parameters on the tilt angle during directional solidification of ternary eutectics, Computational Materials Science 138 (2017) 403–411.
- [50] M. Kellner, J. Hötzer, P. Steinmetz, K. Dargahi Noubary, W. Kunz, B. Nestler, Phase-field study of microstructure evolution in directionally solidified NiAl-34Cr during dynamic velocity changes, Solidification Processing 2017: Proceedings of the 6th Decennial International Conference on Solidification Processing (2017) 372–375.
- [51] M. Bauer, J. Hötzer, M. Jainta, P. Steinmetz, M. Berghoff, F. Schornbaum, C. Godenschwager, H. Köstler, B. Nestler, U. Råde, Massively parallel phase-field simulations for ternary eutectic directional solidification (2015) 8.
- [52] J. A. Dantzig, M. Rappaz, Solidification, EPFL press, 2009.
- [53] LRZ - Leibniz Supercomputing Centre, SuperMUC Petascale System, <https://www.lrz.de/services/compute/supermuc/>, 2019. [Accessed: January 2019].
- [54] A. Lahiri, C. Tiwary, K. Chattopadhyay, A. Choudhury, Eutectic colony formation in systems with interfacial energy anisotropy: A phase field study, Computational Materials Science 130 (2017) 109–120.